RSC Advances

PAPER

View Article Online
View Journal | View Issue

Cite this: *RSC Adv.*, 2016, **6**, 39511

The effect of growing time and Mn concentration on the defect structure of ZnO nanocrystals: X-ray diffraction, infrared and EPR spectroscopy†

Saadet Yildirimcan,[ab] Kasim Ocakoglu,*[ac] Selma Erat,[b] Fatih M. Emen,[d] Sergej Repp[e] and Emre Erdem*[e]

ZnO nanopowder was synthesized *via* a hydrothermal route and characterized with several methods such as XRD, TG/DTA, FT-IR, FE-SEM, TEM and Electron Paramagnetic Resonance spectroscopy (EPR) in order to investigate the effect of growing time and Mn doping on the defects which occurred. The pure ZnO nanopowder was obtained in a hexagonal phase with (101) as the preferred orientation except for the one prepared for 36 h which is (002). The growing time does effect the orientation of the crystallite whereas the Mn-doping does not. The concentration of Mn^{2+} significantly increases the spin–spin interaction in the ZnO : Mn nanopowder. It was observed that there was a competition between intrinsic (Zn and O vacancies) and extrinsic (Mn^{2+} ion) structural defects but still the former defects are dominant in ZnO : Mn. The effect of growing time and concentration of Mn^{2+} on the activation energy of ZnO and the ZnO : Mn nanopowder are calculated by Kissinger–Akahira–Sunose (KAS) and Flynn–Wall–Ozawa (FWO) methods.

Received 15th February 2016
Accepted 11th April 2016

DOI: 10.1039/c6ra04071c

www.rsc.org/advances

1. Introduction

Zinc oxide (ZnO) is an attractive material particularly in the area of electronics, photonics, acoustics and sensing. ZnO having a wide-bandgap (E_g = 3.37 eV) energy is a transparent semiconductor to visible light that is appropriate for short wavelength optoelectronic applications and has a large exciton binding energy (60 meV) which allows efficient excitonic emission at room temperature (RT).[1] ZnO nanostructured materials have attracted considerable interest from scientists because of their remarkable performance in a broad range of high technology applications such as surface acoustic wave filters,[2] photonic crystals,[3] photodetectors,[4] light emitting diodes,[5] photodiodes,[6] gas sensors,[7] optical modulator waveguides,[8] room-temperature ultraviolent (UV) lasers[9] and solar cells.[10,11] There are several techniques to synthesize ZnO nanocrystals such as sol–gel processing,[12] high-energy[13] and cryogenic ball-milling,[14] microwave-assisted synthesis,[15] wet chemical,[16] hydrolysis/condensation,[17] aerosol spray analysis[18] and hydrothermal synthesis.[19] Among these techniques, hydrothermal synthesis of growing ZnO nanocrystals has gained immense popularity because it is a cheap and easy method and does not need necessarily complex devices.[20] Intrinsic defects in ZnO material can be listed as follows: zinc vacancy V_{Zn}, oxygen vacancy V_O, interstitial zinc Zn_i interstitial oxygen O_i, and antisite oxygen O_{Zn}. Because of the recombination of free excitons ZnO exhibits one typical emission peak in the UV-region and one or more defect-related emission peaks in the visible-light region.[21] The origin of defect-related emission is still not very well understood and it is controversially discussed in literature.[21–23] There are common hypothesis to explain the different defect emissions (violet, blue, green, yellow and orange-red) but the chemical natures of the defects responsible for these emissions are still missing. For example, it is attributed that the yellow emission caused by oxygen interstitial defects. The presence of $Zn(OH)_2$ at the surface possibly occurs weak UV and the strong visible (broad yellow and green) emission peak. In addition, the orange-red emission (640–650 nm) is commonly attributed to the presence of excess oxygen in the samples (oxygen interstitial defects)[24] or surface dislocations[25] or zinc interstitial.[26] Recently, Motaung *et al.* nicely showed that zinc and oxygen related defects play a crucial role in mediating ferromagnetism in the undoped ZnO.[18] On the other hand doping ZnO with transition metal elements like Fe, Co, Mn or Cr leads to materials with entirely different behavior towards magnetic and optical excitation. This new research direction is

[a]*Advanced Technology, Research and Application Center, Mersin University, Mersin, TR-33343, Turkey. E-mail: kasim.ocakoglu@mersin.edu.tr*

[b]*Faculty of Engineering, Department of Electrical-Electronics Engineering, Toros University, TR-33140 Mersin, Turkey*

[c]*Department of Energy Systems Engineering, Faculty of Technology, Mersin University, TR-33480 Tarsus, Mersin, Turkey*

[d]*Faculty of Arts and Sciences, Department of Chemistry, Mehmet Akif Ersoy University, TR-15030 Burdur, Turkey*

[e]*Institut für Physikalische Chemie, Albert-Ludwigs-Universität Freiburg, Albertstr. 21, 79104 Freiburg, Germany. E-mail: emre.erdem@physchem.uni-freiburg.de*

† Electronic supplementary information (ESI) available. See DOI: 10.1039/c6ra04071c

named as diluted magnetic semiconductors (DMS).[27,28] DMS materials which are based on ZnO could show not only ferromagnetism at RT upon doping with transition metal ions, *e.g.* (Fe^{3+}),[29] (Cr^{3+}),[30] (Co^{2+}),[31] and (Mn^{2+})[16,18,32] but also simultaneously exhibit ferromagnetic and semiconducting properties.[28] Recently, Mn doped ZnO revealed ferromagnetism above RT[33] which is important for the new spintronic devices (spin LED's, spin valve transistors) and magneto-optic components. Contrarily, there are also works[34] reporting that there is no indication of ferromagnetism nor antiferromagnetism in Mn doped ZnO. Interestingly, Toloman *et al.* reported that Mn doped ZnO synthesized *via* wet chemical route revealed ferromagnetism in the low temperature annealed samples and disappears in the samples thermally treated at high temperatures.[16] Due to lack of advanced electron paramagnetic resonance (EPR) studies and insufficient characterization of the materials there is ongoing controversy[28,33,34] regarding the magnetic properties of ZnO based DMS. We believe that this study may contribute to the magnetic studies as complementary information. Here, magnetic properties of ZnO were excluded and we focused on more to the synthesis and characterization of the electronic and thermal properties. More specifically, we are scoping not only to understand structural changes in ZnO *via* Mn doping but also investigate the changes of local environment of doped ion Mn^{2+}. Moreover, it is expected to get kinetic information about the structures by the aid of detailed thermal analysis.

2. Experimental section

2.1. Synthesis of the ZnO and ZnO : Mn nanopowders

The zinc nitrate hexahydrate ($Zn(NO_3)_2 \cdot 6H_2O$, Acros Organics), polyethylene glycol (PEG300, Aldrich Chemistry) and ammonia (NH_3, Analar Normapur) were used as precursors to produce ZnO nanopowders by the aid of hydrothermal technique. The experiments were performed in a Teflon-lined DAH-904 autoclave (DAH-904). 2.97 g of $Zn(NO_3)_2 \cdot 6H_2O$ was dissolved in 100 mL of distilled water, and then 3.36 g PEG300 was added into the solution. The pH of the solution, which is important for the nanopowder formation, was adjusted to 10 by addition of (NH_3).[35,36] The resulting solution was kept in Teflon-lined autoclave at 70 °C for various duration times such as 1 h, 6 h, 12 h, 24 h and 36 h. After cooling down to RT, the precipitate was filtered, washed with distilled water several times, and dried in an oven at 80 °C for 1 h. The ZnO nanopowders are probably occurred by the following formation subsequent mechanisms:

$$Zn^{2+}_{(aq)} + n\text{PEG} \leftrightarrow [Zn(\text{PEG})_n]^{2+}$$

$$[Zn(\text{PEG})_n]^{2+} + 4OH^-_{(aq)} \leftrightarrow [Zn(OH)_4]^{2-} + n\text{PEG}$$

$$[Zn(OH)_4]^{2-} \leftrightarrow ZnO\downarrow + 2H_2O$$

where n is an integer. The Zn source was primarily in the form of $[Zn(\text{PEG})_n]^{2+}$; and the remaining Zn source existed in the form of $[Zn(OH)_4]^{2-}$.[37] Finally, further ZnO is obtained by decomposition of $[Zn(OH)_4]^{2-}$.

The Mn-doped ZnO nanopowder was also synthesized with the same technique. The $Mn(NO_3)_2 \cdot 4H_2O$ solution was added into the solution of which is used to prepare ZnO nanopowder (6 h). A certain concentration of $Mn(NO_3)_2 \cdot 4H_2O$ solution was calculated according to these conditions. The Mn doped solution was kept in Teflon-lined autoclave at 70 °C for 6 h, and then the precipitation was filtered, washed with distilled water, and were dried in an oven at 80 °C for 1 h. Same procedure was repeated for various Mn^{2+} concentrations (X1: undoped, X2: 5×10^{-4} mol; X3: 10×10^{-4} mol; X4: 25×10^{-4} mol; X5: 75×10^{-4} mol; X6: 100×10^{-4} mol; X7: 250×10^{-4} mol) of ZnO. It is obvious that the similar formation mechanisms will be followed to obtain ZnO : Mn nanopowders. It was observed that once the concentration of Mn^{2+} is increased, the color of the powders changes from light-grey to dark-grey.

2.2. Characterization of the ZnO and ZnO : Mn nanopowders

X-ray powder diffraction patterns were collected with a Bruker D8 Advanced Series powder diffractometer at ambient temperature (40 kV, 40 mA, CuK_α $\lambda = 1.5405$ Å) in steps of 0.03° for 30° $\leq 2\theta \leq$ 80°. Fourier transform infrared (FTIR) spectroscopy measurements of nanopowders were acquired using Perkin Elmer spectrometer with ATR unit. The differential thermal analysis (DTA) and thermogravimetric (TG) curves were recorded by using Seiko SII TG/DTA 7200 equipped with DTA and TG units. The thermal analyses were carried out in the temperature range of 30–1155 °C using α-Al_2O_3 as a reference material while samples were in Pt crucibles. Measurements were performed under the dynamic nitrogen atmosphere with a flow rate of 50 mL min^{-1} and with different heating rates such as 5 °C min^{-1}, 10 °C min^{-1} and 15 °C min^{-1}. Field emission-scanning electron microscopy (FE-SEM) images were recorded using a Zeiss/Supra 55 FE-SEM, and the samples were coated with Pt before the FE-SEM measurements. TEM images of Mn doped ZnO nanopowder were recorded using a JEOL-JEM-1011 transmission electron microscope (Jeol LTD., Tokyo, Japan), and pictured by Megaview III digital camera (Olympus Soft Imaging Solutions GmbH, Munster, Germany). Before the TEM pictures were recorded, the nanopowder was dispersed in ethanol and placed on a 300 mesh formvar-coated copper grid and finally dried in open air. The TEM microscope was operated at an accelerating voltage of 100 kV. The elemental analyses of the Mn doped ZnO nanopowders were carried out by Energy Dispersive X-ray (EDX) spectroscopy technique. The spectra were collected using Zeiss, SUPRA-55 FE-SEM equipped with an Energy Dispersive X-ray Spectrometer. Furthermore, considering the typical detection limit for EDX, the Mn concentration was also determined by using inductively coupled plasma mass spectrometry (ICP-MS) (Agilent 7500ce (Tokyo, Japan)). For ICP-MS measurements, the Mn : ZnO nanopowders were dissolved using the mixture of acid solution (3 mL of HCl 37% + 1 mL of HNO_3 65%). The EDX diffractograms and the elemental percentage of Mn, and the results of the ICP-MS are given as ESI (Table S1†). X-band (9.47 GHz) and

Q-band (34.2 GHz) continuous-wave EPR measurements were done with Bruker EMX and ESP380 spectrometers, respectively, using rectangular TE102 (X-band) and dielectric-ring TE011 (Q-band) resonators (both from Bruker) at RT. The off-set in magnetic-field were determined with polycrystalline DPPH (2-diphenyl-1-picrylhydrazyl) of known *g*-factor ($g = 2.0036$).

3. Results and discussion

3.1. Structural analysis of the ZnO and ZnO : Mn nanopowders

The XRD patterns of the ZnO nanopowders produced for various growing time and Mn^{2+} doping levels are shown in Fig. 1(a), enlarged in Fig. 1(b) and (c) and enlarged in Fig. 1(d), respectively.

It is obvious that the sharp diffraction patterns indicates the well crystalline structure for ZnO and ZnO : Mn samples. All the patterns of ZnO were indexed to hexagonal wurtzite structure with the space group of $P6_3mc$ (186) (JCPDS no.: 36-1451). The lattice parameters (a, c) of the ZnO nanopowder were calculated using the XRD data along with Bragg law ($2d \sin\theta = n\lambda$) ($n = 1$; λ is the wavelength of incident X-ray used) and following formula, which is defined for hexagonal phase:

$$\frac{1}{d^2} = \frac{4}{3}\left[\frac{h^2 + hk + k^2}{a^2}\right] + \frac{l^2}{c^2} \quad (1)$$

where d is the distance between two different planes and (hkl) are the Miller indexes. The calculated values were listed in Table 1.

The crystallinity of the powder increases with increasing growing time, as it is clear to see that the diffraction peaks become sharper. The (101) direction is the most preferred direction for all the samples except for the sample prepared for 36 h. The 36 h sample was grown with the preferred direction of (002) and showed the highest intensity in this series. The crystallite size of the samples was determined from X-ray diffraction data where we prefer to use the standard (100) reflection at around $2\theta = 31.90^\circ$ because of its highest intensity. We apply the Scherrer's formula[38] in order to quantify the average crystallite size of nanopowders.

The calculated crystallite sizes are 30 nm, 33 nm, 36 nm, 39 nm and 51 nm for 1 h, 6 h, 12 h, 24 h and 36 h, respectively. Thus, the crystallite size of ZnO increases upon growing time increases.

The crystal structure of Mn^{2+} doped ZnO was also characterized *via* XRD pattern and are shown in Fig. 1(c) and its expanded view of (100), (002) and (101) peaks in Fig. 1(d). The diffraction peaks of Mn^{2+} doped ZnO were also indexed to hexagonal structure without any impurity peaks (JCPDS no.: 03-0888). It is revealed that the wurtzite structure is not affected by Mn^{2+} doping. The unit cell parameters were calculated and given in Table 2. Slight differences were observed in the lattice constants compared to those of undoped ZnO; $a = 3.2358$ Å, $c = 5.2840$ Å.

The XRD peak slightly shifted toward a lower angle with increased Mn concentration. This shows the increase of the lattice parameters. The ionic radius of Mn^{2+} (97 pm) is larger than that of Zn^{2+} (88 pm) in six-fold coordination. Thus, it is expected that the cell parameters are increased *via* Mn^{2+} doping. The undoped sample X1 has cell parameter $a = 3.2358$ Å which increases up to 3.2685 Å for the sample X7 which has the highest doping concentration. On the other hand, the effect the Mn concentration on the crystallite size is not clear as the effect of the growing time. This is because the change in the β (full width at half maximum of XRD profile) does not proportional with the Mn^{2+} concentration. The calculated crystallite sizes are 32 nm, 33 nm, 21 nm, 33 nm, 31 nm and 35 nm for X2, X3, X4, X5, X6, and X7, respectively. Here we do not observe any systematic increase of size by increasing the Mn doping. This may due to the in homogeneous distribution of Mn ions. On one side, below certain amount of Mn concentrations, some part of the nanocrystals statistically are not doped, on the other side the remaining part contain only one Mn ion, which seems to deviate the particle size randomly. Moreover adding Mn ions changes the morphology which has great impact on the size.

3.2. FT-IR analysis of the ZnO and ZnO : Mn nanopowders

FT-IR was used for the detailed structural analysis of ZnO nanopowders. The FT-IR spectra of undoped ZnO nanopowder synthesized at different time intervals and doped with various Mn^{2+} concentrations are shown in Fig. 2(a and b), enlarged in Fig. 2(c) and (d). The observed vibration bands between 2300 cm^{-1} and 2400 cm^{-1} are assigned to the CO_2 mode in air.[39] The symmetric and asymmetric $-CH_2$ stretching modes locate between 2800 cm^{-1} and 3000 cm^{-1}.[40] While the characteristic bands of 3500–3800 cm^{-1} were corresponded to stretching vibration of H_2O, the observed bands at 1072 cm^{-1} and 1030 cm^{-1} were attributed to the bending vibrations of –OH groups.[41] The peak at 1131 cm^{-1} is ascribed to O–H stretching vibration of H_2O in Mn–Zn–O lattice.[39] The symmetric stretching occurs between 818 cm^{-1} and 956 cm^{-1} and corresponds to the vibration of $(NO_3)^{-1}$ ions.[40] The characteristic FT-IR peaks in the region below 1000 cm^{-1} is very important to understand the presence of Zn–O bond and the functional groups. Since, the vibrational modes of the metal–oxygen are expected in this region. The vibration bands observed in the range of 470–560 cm^{-1} were ascribed to the vibration of Zn–O.[41] Also, the vibration bands observed in the range of 470–680 cm^{-1} are attributed to the stretching modes of Zn–Mn–O.[39] Besides, the sharp band observed below 1000 cm^{-1} in the spectrum of the Mn doped ZnO nanostructures is due to the Mn^{2+} ions implantation into the ZnO structure. These results highly suggest the incorporation of Mn^{2+} into ZnO lattice. Also, there is no absorption peak at 609 cm^{-1} which is characteristic for manganese oxides.[42] The FT-IR peaks and their assignments of ZnO and ZnO : Mn nanopowder are presented in Table 3.

3.3. Thermal analysis of the ZnO : Mn nanopowders

The thermal properties of Mn-doped ZnO nanopowder (X2, X3, X4, X5, X6 and X7) were studied by thermogravimetric analysis from an ambient temperature up to 700 °C under nitrogen

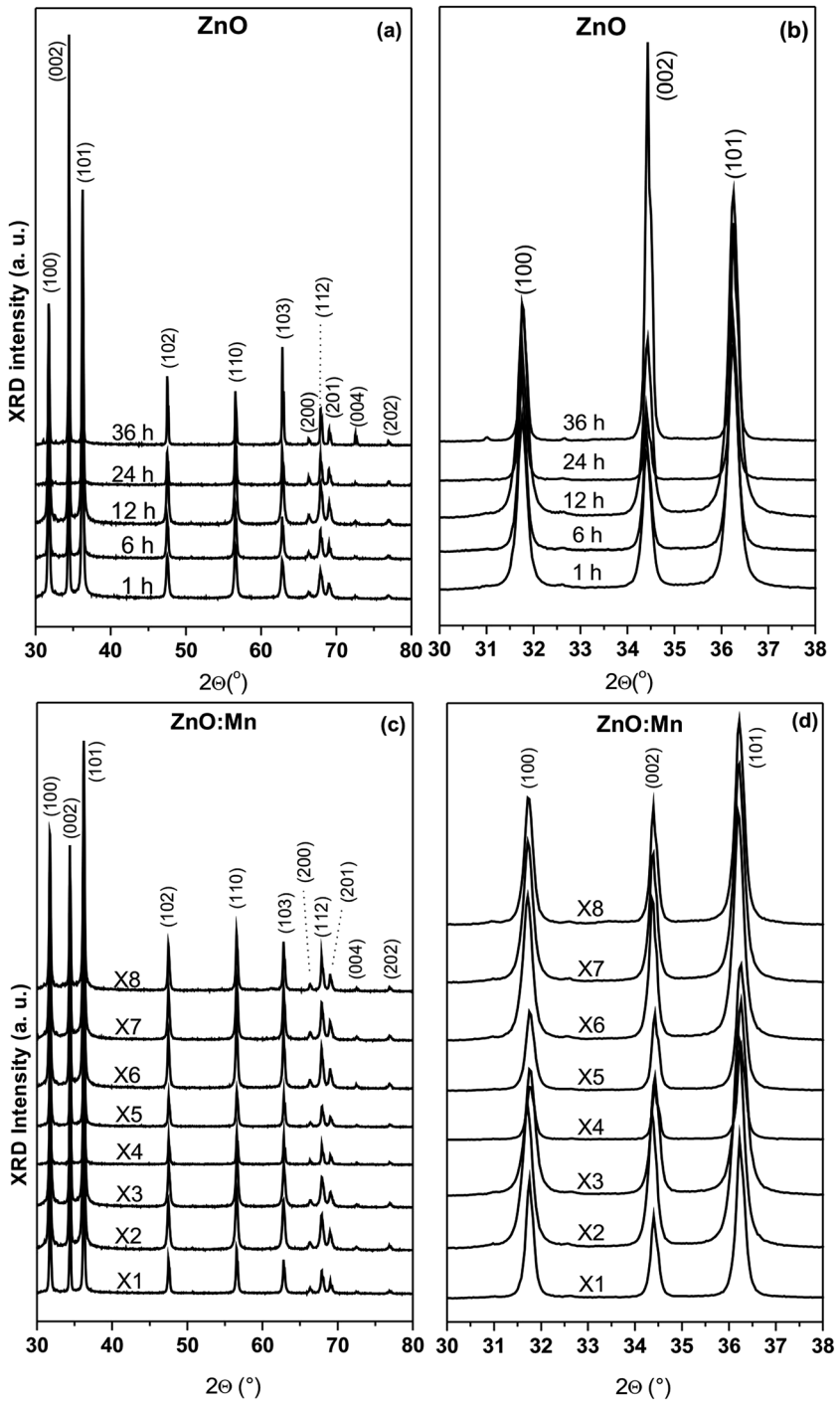

Fig. 1 (a) X-ray patterns of ZnO nanopowder depending on growing time; (b) expanded view of (100), (002) and (101) peaks in all of the samples; (c) X-ray patterns for Mn doped ZnO nanopowders depending on Mn concentration; (d) expanded view of (100), (002) and (101) peaks in all of the samples.

atmosphere. The TG/DTA curves of all samples are shown in Fig. 3(a) and (b).

The thermal decompositions of all compounds occur step by step. The TG/DTA curves of X2 are shown in Fig. 3(a) and (b). The weight losses of X2 occur in two steps. The first steps are in the range of room temperature to 140 °C with weight loss of 2.61% for X2 demonstrating the dehydration of surface-adsorbed water and decomposition of hydroxide groups. The second step occurs in the temperature range of 140–700 °C with weight loss of 1.72% for X2 indicating the decomposition of PEG and other impurities. The DTA curves have an obvious endothermic peak between 99 °C and 153 °C for X2 with a maximum around 164 °C, which demonstrate that the decomposition of OH^- groups and the removal of adsorbed

Table 1 The lattice parameters of the ZnO nanopowder prepared with different growing time

	Lattice parameters (Å)	
Growing time (h)	*a*	*c*
1	3.2342	5.2815
6	3.2358	5.2840
12	3.2340	5.2813
24	3.2225	5.2625
36	3.2194	5.2573

Table 2 The lattice parameters of ZnO : Mn prepared with different Mn concentration

	Lattice parameters (Å)	
Mn concentration (mol)	*a*	*c*
X1 (undoped)	3.2358	5.2840
X2	3.2360	5.2845
X3	3.2370	5.2860
X4	3.2440	5.2974
X5	3.2475	5.3030
X6	3.2650	5.3317
X7	3.2685	5.3375

water take place simultaneously. These results are in agreement with the characteristics of ZnO nanoparticles reported in literature.[43,44] According to formation mechanism, ZnO is obtained by decomposition of $[Zn(OH)_4]^{2-}$. It is expected that the OH^- ions and H_2O molecules have been adsorbed on the surface of formed ZnO nanopowders. We estimated that the amount of adsorbed OH^- ions and H_2O molecules for X2 sample is greater than others (X3–X7). The Mn doped ZnO samples (X3, X4, X5, X6 and X7) show similar decomposition characteristics: the first decompositions are shown with weight loss of 1.75% for X3, 1.16% for X4, 2.4% for X5, 2.36% for X6 and 2.36% for X7, respectively from room temperature to the range of 477–486 °C are mainly due to the removal of physically and chemically adsorbed water, the decomposition of the hydroxide group on the surface of the nanopowder.[45,46] The second decompositions are observed with weight loss of 0.4% for X3, 0.42% for X4, 0.43% for X5, 0.4% for X6 and 0.39% for X7 from 330 to 700 °C. The observed weight losses are due to the decomposition of PEG and other impurities. The DTA curves of X3–X7 show wide endothermic peaks between 30 °C and 250 °C which demonstrate that the decomposition of OH^- groups and the removal of adsorbed water. The others are attributed to the decompositions of PEG and impurities. The TG results indicate the presence of PEG on the sample surface. These results are consistent with given earlier FT-IR results.

3.4. Kinetic analysis of the ZnO : Mn nanopowder

The activation energies of all compounds were calculated except of the last stages. Kinetic investigation of the last decomposition stages cannot be realized due to the fast reaction and

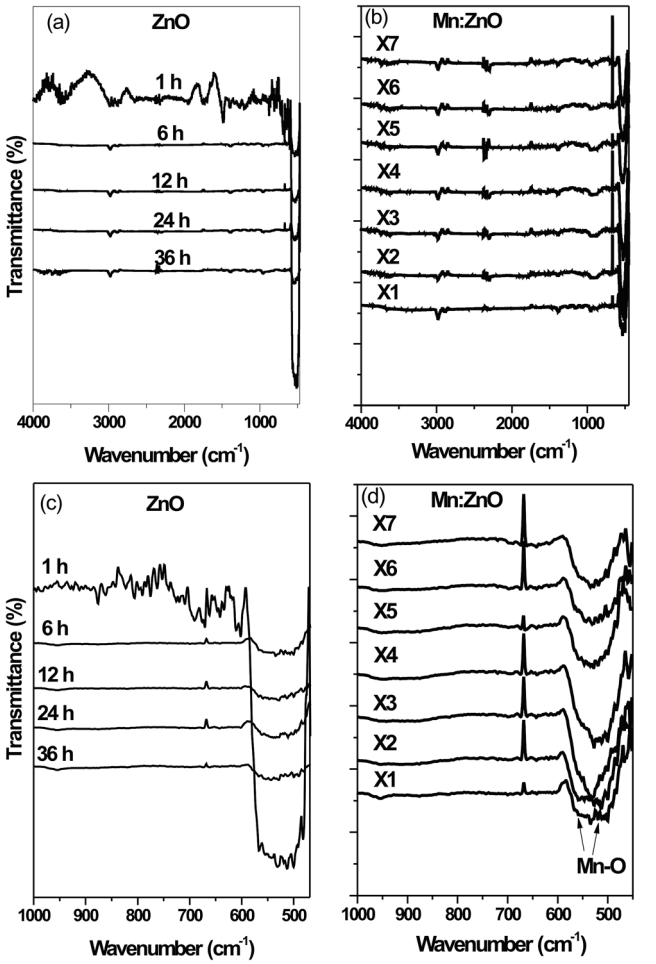

Fig. 2 (a) FT-IR spectra of ZnO nanopowder depending on growing time, (b) FT-IR spectra of Mn doped ZnO nanopowder depending on Mn concentration, (c) enlarged view of ZnO nanopowder depending on growing time, (d) enlarged view of Mn doped ZnO nanopowder.

irregular temperature data.[47] The Kissinger–Akahira–Sunose (KAS) and Flynn–Wall–Ozawa (FWO) methods which are well known as model free isoconversional methods were used to calculate the activation energies of the compounds. The main assumption of these methods is that the reaction mechanism does not change with reaction conversion (α), temperature and heating rate. The final equations of these methods are given in following:[48–50]

FWO equation:

$$\ln \beta = \left[\frac{AE_a}{Rg(\alpha)}\right] - 5.3305 - 1.05178\frac{E_a}{R}\frac{1}{T} \quad (2)$$

and KAS equation:

$$\ln \frac{\beta}{T^2} = \left[\ln \frac{AR}{g(\alpha)E_a}\right] - \frac{E_a}{R}\frac{1}{T} \quad (3)$$

where, α is the degree of conversion, A is the pre-exponential factor, β is heating rate, T is absolute temperature, E_a is the activation energy, $g(\alpha)$ is an unknown function of the conversion, and R is the gas constant. The graphs of $\ln \beta$ *versus* $1/T$ (for

Table 3 FT-IR frequencies obtained for ZnO and Mn doped ZnO nanopowder

Wavenumber (cm^{-1})	Assignment
3500–3800 (both)	Stretching vibration of H_2O
2800–3000 (both)	Symmetric and asymmetric $-CH_2$ stretching modes
2300–2400 (both)	CO_2 molecule
1131 (only Mn : ZnO)	O–H stretching vibration of H_2O
1072 and 1030 (both)	Bending vibrations of –OH groups
818–956 (both)	Symmetric stretching vibration of NO_3^{-1} ions
470–560 (only undoped ZnO)	Vibration of Zn–O
470–680 (only Mn : ZnO)	Stretching modes of Zn–Mn–O

FWO equation), and the graphs of ln β/T^2 *versus* $1/T$ (for KAS equation) are plotted. Apparent activation energies, E_a of the decomposition reactions for the conversion degree, α varying in the range of 0.05–0.95 in a step of 0.05 can be calculated with using of slope values of these graphs. Kinetics Committee of the International Confederation for Thermal Analysis and Calorimetry (ICTAC) has recommended to determine the E_a values in a wide range of a between 0.05 and 0.95 with increments of 0.05.[41] The E_a values obtained using the FWO methods are higher than that of obtained using KAS method. The E_a *versus* α graphs for all compounds based on model-free KAS and FWO methods are shown in Fig. 4.

The E_a values of the X2 increase up to $\alpha = 0.1$ and remain relatively constant in the conversion degree between 0.1 and 0.95. So it can be said that there is only one dominant kinetic process in these range of α. The average E_a values are 127.70 kJ mol^{-1} and 133.97 kJ mol^{-1} calculated using the KAS and FWO methods. The E_a *versus* α graph of the X3 are showing that the E_a values decrease up to $\alpha = 0.1$ and then start to increase up to $\alpha = 0.45$ then again tends to decrease. The average E_a values are 79.91 kJ mol^{-1} and 84.63 kJ mol^{-1} calculated using the KAS and FWO methods. The E_a values of the X4 dramatically increase up from $\alpha = 0.05$ to 0.95. The calculated E_a values are 75.38 kJ mol^{-1} and 78.59 kJ mol^{-1} calculated using the KAS and FWO methods. The E_a values of the X5 increase up to $\alpha = 0.6$ and reach maximum value (278.45 kJ mol^{-1}) and decrease is

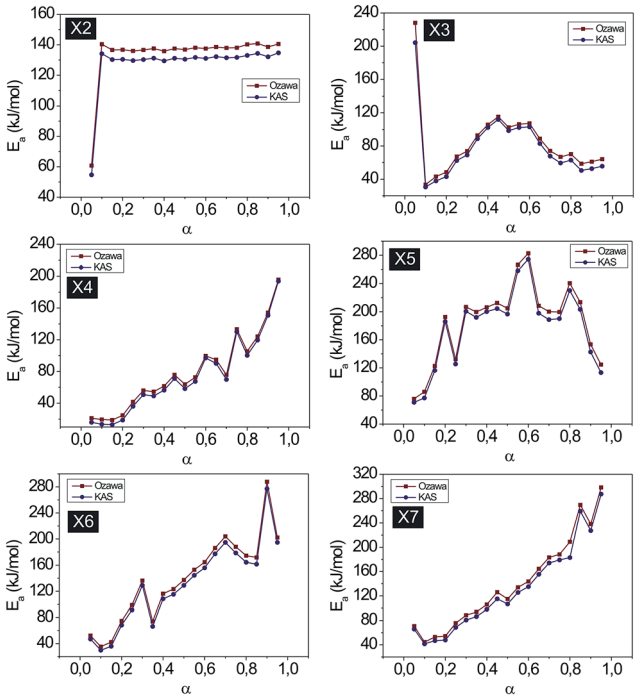

Fig. 4 The E_a *versus* α graphs for all compounds based on model-free KAS and FWO methods.

observed immediately after this decomposition ratio up to $\alpha = 0.95$. The average E_a values are 166.82 kJ mol^{-1} and 183.18 kJ mol^{-1} calculated using the KAS and FWO methods. It is seen that the E_a values of X6 are increasing in irregular. The activation energy values of the X6 increase with an increase in the conversion degree up to $\alpha = 0.25$. A partial decrease is observed immediately after this decomposition ratio, but after then the activation energy increases again and reaches maximum value at $\alpha = 0.90$ (282.52 kJ mol^{-1}). After reaching the maximum value, the activation energy decreases again. The average E_a values are 131.02 kJ mol^{-1} and 136.95 kJ mol^{-1} calculated using the KAS and FWO methods. It is observed that the E_a values persistently increase with an increase in the decomposition ratio for the X7 and then decrease. The average E_a values are calculated as 130.77 kJ mol^{-1} and 138.55 kJ mol^{-1} by the KAS and FWO methods. These results show that there are multi-step

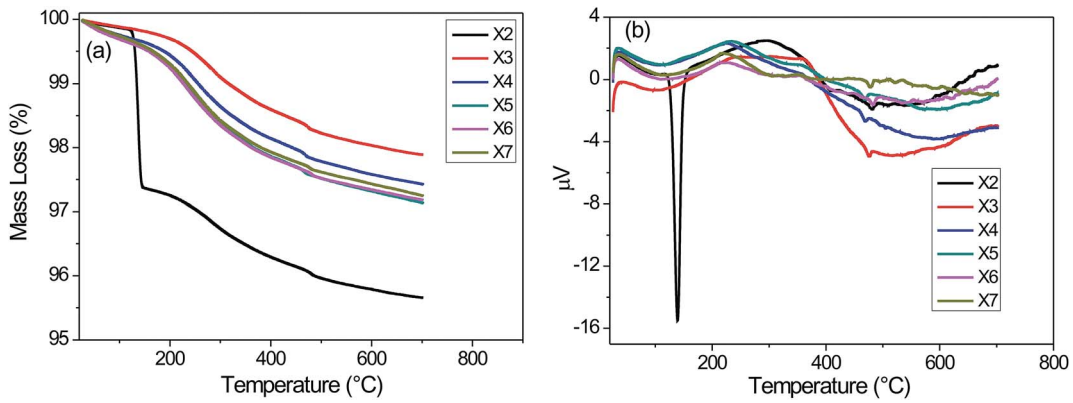

Fig. 3 Thermal gravimetric and differential thermal analysis of ZnO : Mn nanopowder: (a) TG and (b) DTA graphs.

Table 4 The values of the activation energy E_a, of the first decomposition processes

Compounds	FWO method, kJ mol^{-1}	KAS method, kJ mol^{-1}
X2	133.97	127.70
X3	84.63	79.91
X4	78.59	75.38
X5	183.18	166.82
X6	136.95	131.02
X7	138.55	130.77

kinetic processes for X3 to X7. All results are summarized in Table 4.

3.5. Elemantal and microstructure analysis of the ZnO and ZnO : Mn nanopowders

The features of nanomaterials are strongly affected by the chemical composition. The EDX results show chemical composition of the nanoparticles and presence of manganese content (Fig. S1†). The ICP result revealed that the amount of manganese which was incorporated into the ZnO crystal lattice increases proportionally with the amount used in the preparation step for each samples as it was summarized in ESI (Table S1†).

Field emission-scanning electron microscopy (FE-SEM) was used to examine the morphology of the nanopowder. FE-SEM images of the ZnO nanopowder synthesized for different time durations by using hydrothermal method are shown in the Fig. 5.

The powder morphology revealed more or less nanorod shape. The lengths of the nanorods are in the scale of the micrometers (1–7 μm) and their diameters are in the range of 100 to 200 nm. The ZnO nanorods obtained at 1 h time duration are in the pyramid-like structure, whereas the ones obtained at 6 h, 12 h and 36 h are in the nanoneedle form. Finally those synthesized at 24 h are in the form of nanorods. On the other hand, macroscopic images show that generally ZnO nanorods are indeed in the flower-like structure. Fig. 6 shows typical FE-SEM images of the samples synthesized with different concentration of Mn ranging from 5×10^{-4} mol to 250×10^{-4} mol. Fig. 6 reveals a large quantity of well-defined nanorods. These nanorods are of uniform size, smooth surface as shown in the SEM images of the samples. The FE-SEM image reveals that each flower-like structure consisted of closely packed pyramid-like rods. On the other hand, ZnO nanorods composed of nanoneedle-shaped as shown in the SEM images. Especially, while X1 sample resembles nanoneedles, others look like pyramid-like structures. Also, end portions of undoped ZnO nanorods are not in the form of pyramid-like. The diameter of the nanorods gradually becomes smaller along the growth direction. The average diameter and the length of Mn doped ZnO nanorods are 100–200 nm and 1–3 μm, respectively. The diameter is about 70 nm at the tip. The low-magnification FE-SEM image demonstrates that the typical products consist of

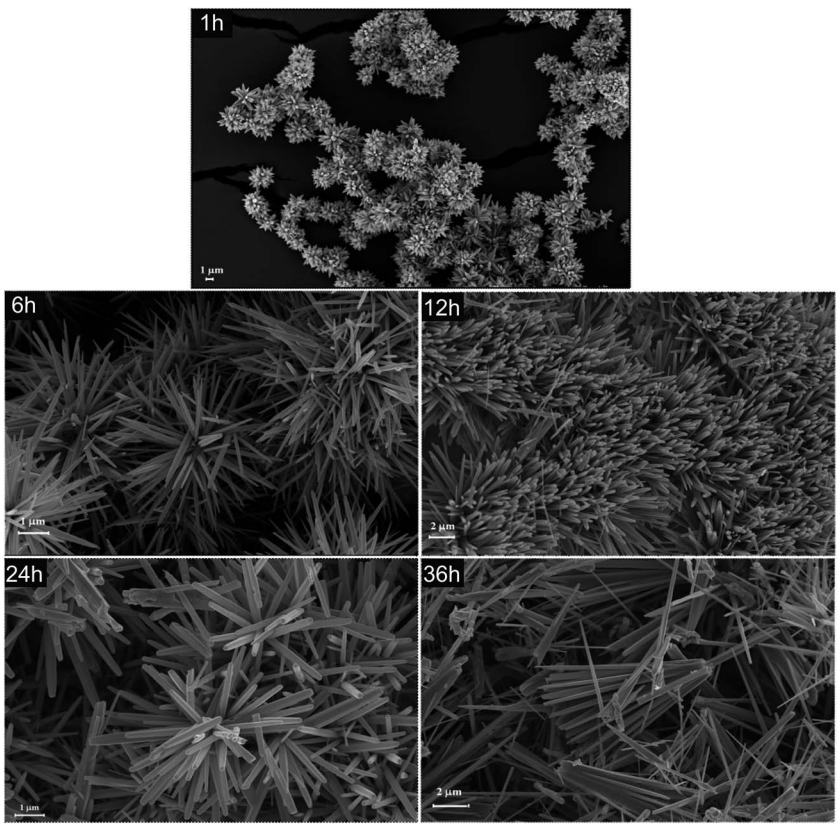

Fig. 5 FE-SEM images of undoped ZnO nanopowder.

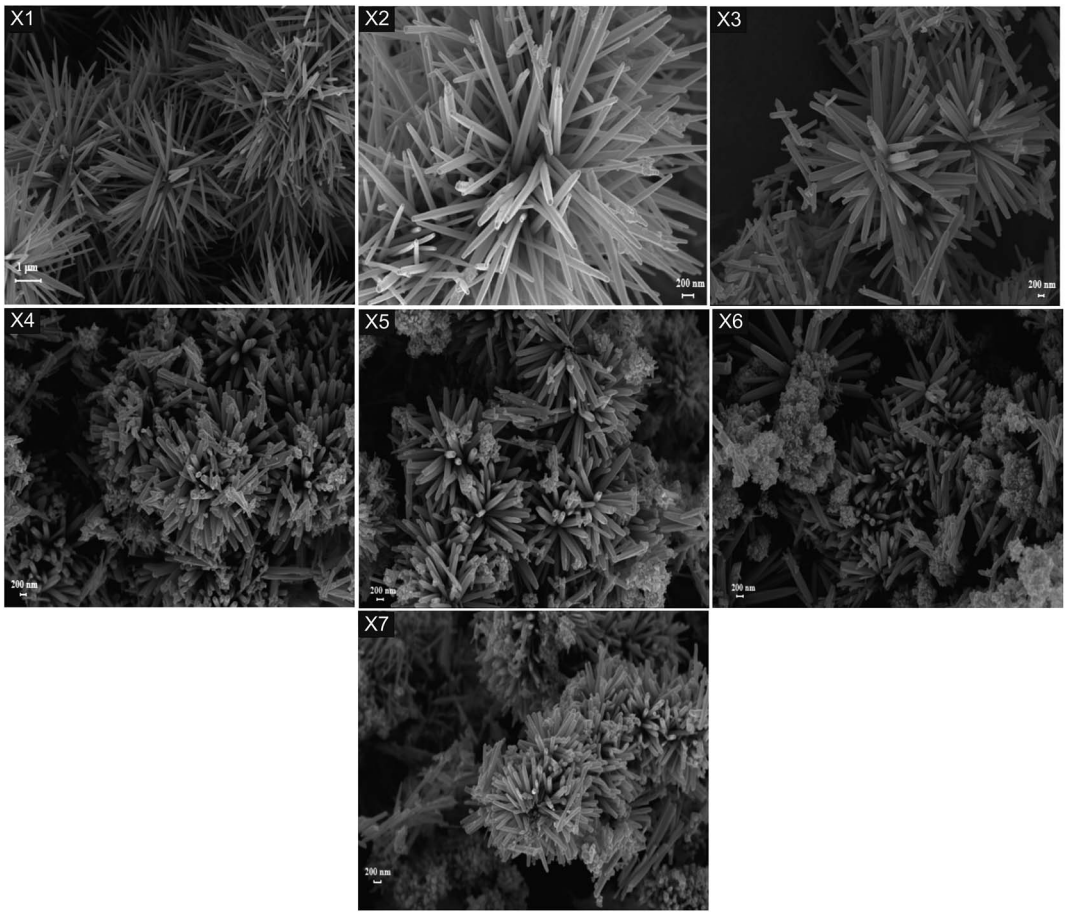

Fig. 6 FE-SEM images of Mn doped ZnO nanopowder.

a large quantity of well-dispersed rods structures. The images show an abundance of nearly flowerlike particles of undoped and Mn-doped ZnO nanorods. It can be seen that Mn doping in ZnO nanorods seems to have small influence on size and the morphology of the as-synthesized samples.

Fig. 7 shows the TEM images of the samples synthesized in different concentration of Mn^{2+} ranging from 5×10^{-4} mol to 250×10^{-4} mol. As it is mentioned before, the FE-SEM images show that the Mn doped ZnO includes both nanoneedles and nanorods structure. The TEM images confirm that this nanopowder was formed mainly in nanorods shape. The diameters of the nanorods are getting smaller along the edge of the rods. It is possible to control the morphologies such as flowerlike, spindlelike, swordlike or umbellarlike structure of ZnO by controlling the reagents used.[37]

3.6. EPR spectroscopy analysis of the ZnO and ZnO : Mn nanopowders

EPR spectroscopy was applied to investigate the influence of the growing time and the Mn concentration on the electronic properties of ZnO samples. The spin-Hamiltonian concept is applied for the theoretical description of the observed EPR spectra. Details of the theoretical background of Mn doped metal oxide has been described by us elsewhere.[51–54] In Fig. 8(a)

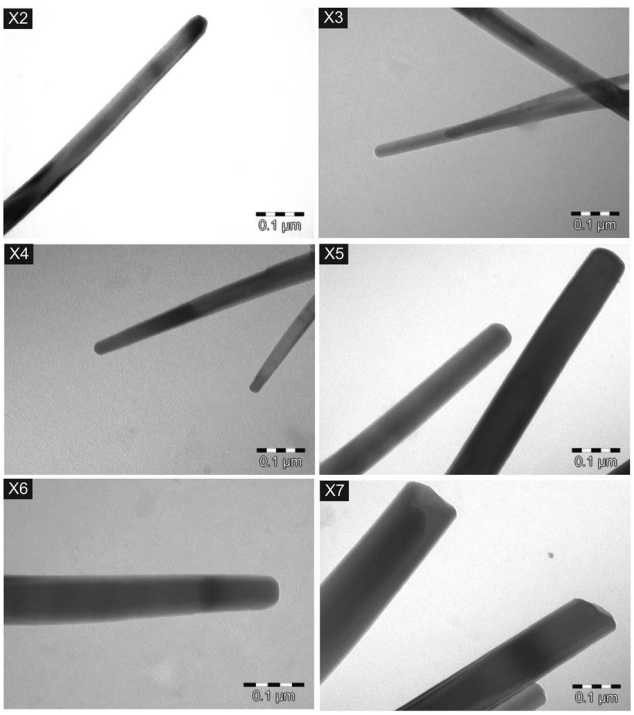

Fig. 7 TEM images of Mn doped ZnO nanopowder.

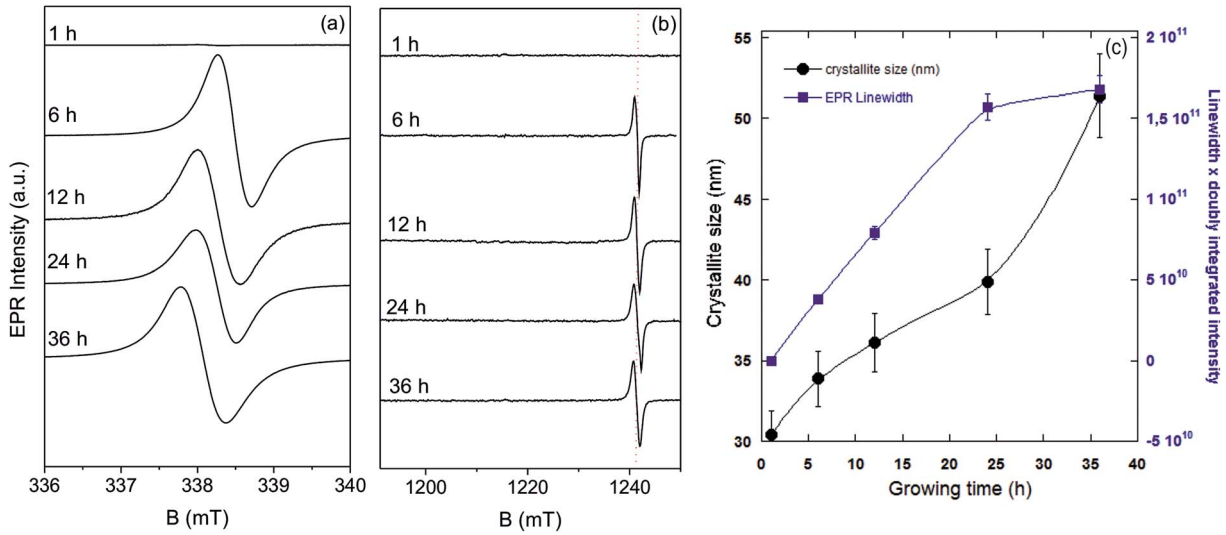

Fig. 8 The EPR spectra of undoped ZnO depending on growing time (a) X band; (b) Q band; (c) comparison of the change in crystallite size and EPR linewidth by growing time deduced from X-band spectra.

and (b) we present EPR results of undoped samples depending on growing time both measured by X and Q band. Except the l h sample, all samples revealed EPR signal at $g = 1.9620$ indicating symmetry breaking oxygen or zinc vacancies {Jakes, 2011 #491; Parashar, 2012 #585}. This shows that 1 h hydrothermal treatment is not enough to reach the formation energy of defects to form intrinsic defects in ZnO crystal. From the X band results the linewidth multiplied by peak area has been calculated and we observed increase of defect concentration by growing time (Fig. 8(c)). The linewidth increase given in Fig. 8(c) can be also attributed to a distortion of crystal field. That shows also the continuous broadening of the EPR lines by increasing hydrothermal treatment time is due to exchange effects. The effects of the growing time on the crystallite size and EPR linewidth are compared in the Fig. 8(c). We conclude that increasing the growing time increases the crystallite size, and further the defects. It is shown in Fig. 9 that the Mn doped samples revealed typical hyperfine resolved sextet line in X5, X6 and X7 samples in Q band spectra. That is an indication that below some certain Mn concentration the Mn^{2+} ions still not incorporating at the ZnO lattice. Due to spin–spin interactions the highest Mn concentrated (X7) sample revealed line broadening compare to X5 and X6. The sample X4 shows the competition between intrinsic and extrinsic defects. It is seen that intrinsic defects still dominate to EPR signal even doping by Mn^{2+} ions. It is known that the defects in crystals particularly on the surface play an important role for catalytic activity.[55,56]

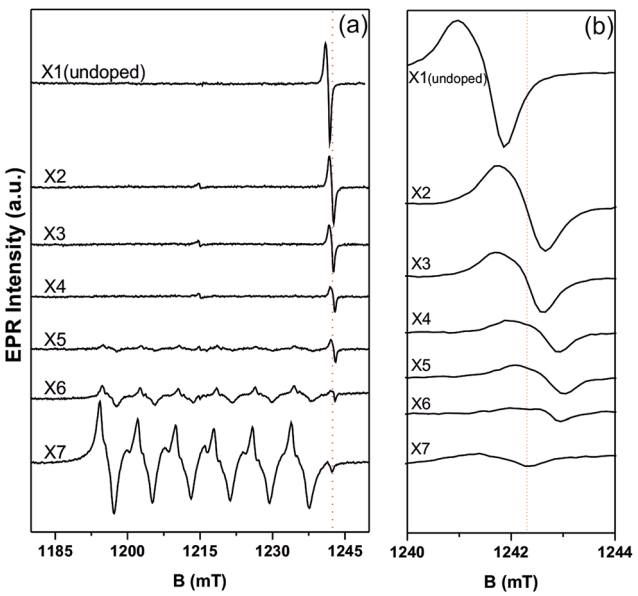

Fig. 9 (a) Q band EPR spectra of Mn doped ZnO samples with different Mn concentrations, (b) expanded view.

4. Conclusions

In this work undoped and doped ZnO nanorods have been synthesized and the structural, thermal and electronic properties were investigated with several methods. We found that crystal structure is pure and Mn ions incorporated in ZnO lattice after certain concentration values. TEM results revealed nicely resolved homogeneously distributed rod shape ZnO nanostructures. By the thermal analysis decomposition of ZnO has been investigated by using two different semi-empirical models. FT-IR results revealed all vibrational modes and these results are totally in agreement with the EPR results. Modifications in crystal structure can be attributed to either intrinsic defects such as oxygen vacancies and Zn vacancies or also the external doping ions Mn^{2+}. The oxidation state of Mn ion also determined as 2+ *via* EPR spectroscopy. Competing effects between intrinsic and extrinsic defects has been investigated and this will contribute to not only to understand the local coordination of Mn^{2+} ions in ZnO lattice but also to determine the solubility limit of Mn^{2+} ions.[57] The change in the crystallite size and EPR linewidth

deduced from X-band spectra upon growing time are compared and correlated. It is observed that both are increased by growing time which is a clear indication of symmetry reduction by increase level of Mn concentration. Also this shows strong spin–spin exchange interaction at higher level of Mn doping. Moreover the intrinsic defects such as vacancies observed in undoped ZnO EPR spectra is quenched *via* Mn doping.

Acknowledgements

This research has been financially supported by the Deutsche Forschunsgemeinschaft, DFG (Grant: Er 662/1-2) and The Scientific and Technological Research Council of Turkey, TUBITAK (Grant: 110M803) in the framework of European Science Foundation (ESF-EUROCORES-EuroSolarFuels-10-FP-006). Continuous support of S. Weber is gratefully acknowledged.

References

1 A. B. Djurisic, W. C. H. Choy, V. A. L. Roy, Y. H. Leung, C. Y. Kwong, K. W. Cheah, T. K. G. Rao, W. K. Chan, H. T. Lui and C. Surya, *Adv. Funct. Mater.*, 2004, **14**, 856–864.
2 N. W. Emanetoglu, C. Gorla, Y. Liu, S. Liang and Y. Lu, *Mater. Sci. Semicond. Process.*, 1999, **2**, 247–252.
3 Y. F. Chen, D. Bagnall and T. F. Yao, *Mater. Sci. Eng., B*, 2000, **75**, 190–198.
4 H. Kind, H. Q. Yan, B. Messer, M. Law and P. D. Yang, *Adv. Mater.*, 2002, **14**, 158.
5 N. Saito, H. Haneda, T. Sekiguchi, N. Ohashi, I. Sakaguchi and K. Koumoto, *Adv. Mater.*, 2002, **14**, 418.
6 J. Y. Lee, Y. S. Choi, J. H. Kim, M. O. Park and S. Im, *Thin Solid Films*, 2002, **403**, 553–557.
7 P. Mitra, A. P. Chatterjee and H. S. Maiti, *Mater. Lett.*, 1998, **35**, 33–38.
8 M. H. Koch, P. Y. Timbrell and R. N. Lamb, *Semicond. Sci. Technol.*, 1995, **10**, 1523–1527.
9 M. H. Huang, S. Mao, H. Feick, H. Q. Yan, Y. Y. Wu, H. Kind, E. Weber, R. Russo and P. D. Yang, *Science*, 2001, **292**, 1897–1899.
10 M. Law, L. E. Greene, J. C. Johnson, R. Saykally and P. D. Yang, *Nat. Mater.*, 2005, **4**, 455–459.
11 A. B. F. Martinson, J. W. Elam, J. T. Hupp and M. J. Pellin, *Nano Lett.*, 2007, **7**, 2183–2187.
12 D. W. Bahnemann, C. Kormann and M. R. Hoffmann, *J. Phys. Chem.*, 1987, **91**, 3789–3798.
13 S. K. S. Parashar, B. S. Murty, S. Repp, S. Weber and E. Erdem, *J. Appl. Phys.*, 2012, **111**, 113712.
14 H. Kaftelen, K. Ocakoglu, S. Tu, R. Thomann, S. Weber and E. Erdem, *Phys. Rev. B: Condens. Matter Mater. Phys.*, 2012, **86**, 014113.
15 J. J. Schneider, R. C. Hoffmann, J. Engstler, A. Klyszcz, E. Erdem, P. Jakes, R. A. Eichel, L. Pitta-Bauermann and J. Bill, *Chem. Mater.*, 2010, **22**, 2203–2212.
16 D. Toloman, A. Mesaros, A. Popa, O. Raita, T. D. Silipas, B. S. Vasile, O. Pana and L. M. Giurgiu, *J. Alloys Compd.*, 2013, **551**, 502–507.
17 A. W. Cohn, K. R. Kittilstved and D. R. Gamelin, *J. Am. Chem. Soc.*, 2012, **134**, 7937–7943.
18 D. E. Motaung, I. Kortidis, D. Papadaki, S. S. Nkosi, G. H. Mhlongo, J. Wesley-Smith, G. F. Malgas, B. W. Mwakikunga, E. Coetsee, H. C. Swart, G. Kiriakidis and S. S. Ray, *Appl. Surf. Sci.*, 2014, **311**, 14–26.
19 W. J. Li, E. W. Shi, Y. Q. Zheng and Z. W. Yin, *J. Mater. Sci. Lett.*, 2001, **20**, 1381–1383.
20 S. Baruah and J. Dutta, *J. Sol-Gel Sci. Technol.*, 2009, **10**, 013001.
21 S. Repp and E. Erdem, *Spectrochim. Acta, Part A*, 2016, **152**, 637–644.
22 A. B. Djurisic, Y. H. Leung, K. H. Tam, Y. F. Hsu, L. Ding, W. K. Ge, Y. C. Zhong, K. S. Wong, W. K. Chan, H. L. Tam, K. W. Cheah, W. M. Kwok and D. L. Phillips, *Nanotechnology*, 2007, **18**, 095702.
23 E. Erdem, *J. Alloys Compd.*, 2014, **605**, 34–44.
24 X. Liu, X. H. Wu, H. Cao and R. P. H. Chang, *J. Appl. Phys.*, 2004, **95**, 3141–3147.
25 H. J. Fan, R. Scholz, F. M. Kolb, M. Zacharias, U. Gosele, F. Heyroth, C. Eisenschmidt, T. Hempel and J. Christen, *Appl. Phys. A: Mater. Sci. Process.*, 2004, **79**, 1895–1900.
26 G. Manabu, O. Naoko, O. Kenichi and K. Mikio, *Jpn. J. Appl. Phys.*, 2003, **42**, 481.
27 V. Avrutin, N. Izyumskaya, U. Ozgur, D. J. Silversmith and H. Morkoc, *Proc. IEEE*, 2010, **98**, 1288–1301.
28 I. Djerdj, G. Garnweitner, D. Arcon, M. Pregelj, Z. Jaglicic and M. Niederberger, *J. Mater. Chem.*, 2008, **18**, 5208–5217.
29 S. Q. Zhou, K. Potzger, G. Talut, H. Reuther, K. Kuepper, J. Grenzer, Q. Y. Xu, A. Mucklich, M. Helm, J. Fassbender and E. Arenholz, *J. Phys. D: Appl. Phys.*, 2008, **41**, 105011.
30 L. B. Duan, X. R. Zhao, J. M. Liu, T. Wang and G. H. Rao, *Appl. Phys. A: Mater. Sci. Process.*, 2010, **99**, 679–683.
31 N. Akdogan, A. Nefedov, K. Westerholt, H. Zabel, H. W. Becker, C. Somsen, R. Khaibullin and L. Tagirov, *J. Phys. D: Appl. Phys.*, 2008, **41**, 165001.
32 Q. Y. Xu, H. Schmidt, L. Hartmann, H. Hochmuth, M. Lorenz, A. Setzer, P. Esquinazi, C. Meinecke and M. Grundmann, *Appl. Phys. Lett.*, 2007, **91**, 092503.
33 P. Sharma, A. Gupta, K. V. Rao, F. J. Owens, R. Sharma, R. Ahuja, J. M. O. Guillen, B. Johansson and G. A. Gehring, *Nat. Mater.*, 2003, **2**, 673–677.
34 J. Alaria, P. Turek, M. Bernard, M. Bouloudenine, A. Berbadj, N. Brihi, G. Schmerber, S. Colis and A. Dinia, *Chem. Phys. Lett.*, 2005, **415**, 337–341.
35 J. Qiu, B. Weng, L. Zhao, C. Chang, Z. Shi, X. Li, H.-K. Kim and Y.-H. Hwang, *J. Nanomater.*, 2014, **2014**, 211.
36 J. Zhang, L. Sun, J. Yin, H. Su, C. Liao and C. Yan, *Chem. Mater.*, 2002, **14**, 4172–4177.
37 X. Wang, Q. Zhang, Q. Wan, G. Dai, C. Zhou and B. Zou, *J. Phys. Chem. C*, 2011, **115**, 2769–2775.
38 S. Erat, H. Metin and M. Arä, *Mater. Chem. Phys.*, 2008, **111**, 114–120.
39 M. Ashokkumar and S. Muthukumaran, *Opt. Mater.*, 2014, **37**, 671–678.
40 N. Rajamanickam, R. N. Mariammal, S. Rajashabala and K. Ramachandran, *J. Alloys Compd.*, 2014, **614**, 151–164.

41 L.-H. Li, J.-C. Deng, H.-R. Deng, Z.-L. Liu and L. Xin, *Carbohydr. Res.*, 2010, **345**, 994–998.
42 M. Pashchanka, R. C. Hoffmann, O. Burghaus, B. Corzilius, G. Cherkashinin and J. J. Schneider, *Solid State Sci.*, 2011, **13**, 224–231.
43 V. I. Anisimkin, M. Penza, A. Valentini, F. Quaranta and L. Vasanelli, *Sens. Actuators, B*, 1995, **23**, 197–201.
44 J. M. Wang and L. Gao, *Inorg. Chem. Commun.*, 2003, **6**, 877–881.
45 V. I. Anisimkim, M. Penza, A. Valentini, F. Quaranta and L. Vasanelli, *Sens. Actuators, B*, 1995, **23**, 197–201.
46 M. Li, B. Hari, X. Lv, X. Ma, F. Sun, L. Tang and Z. Wang, *Mater. Lett.*, 2007, **61**, 690–693.
47 M. Ak, G. K. Çılgı, F. D. Kuru and H. Cetişli, *J. Therm. Anal. Calorim.*, 2012, **111**, 1627–1632.
48 H. Cetişli, G. K. Çılgı and R. Donat, *J. Therm. Anal. Calorim.*, 2012, **108**, 1213–1222.
49 N. Chaiyo, R. Muanghlua, S. Niemcharoen, B. Boonchom, P. Seeharaj and N. Vittayakorn, *J. Therm. Anal. Calorim.*, 2011, **107**, 1023–1029.
50 G. K. Cilgi, H. Cetisli and R. Donat, *J. Therm. Anal. Calorim.*, 2012, **110**, 127–135.
51 E. Aksel, P. Jakes, E. Erdem, D. M. Smyth, A. Ozarowski, J. van Tol, J. L. Jones and R.-A. Eichel, *J. Am. Ceram. Soc.*, 2011, **94**, 1363–1367.
52 E. Erdem, M. Drahus, R. A. Eichel, A. Ozarowski, J. Van Tol and L. C. Brunel, *Ferroelectrics*, 2008, **363**, 39–49.
53 H. Kaftelen, M. Tuncer, S. Tu, S. Repp, H. Gocmez, R. Thomann, S. Weber and E. Erdem, *J. Mater. Chem. A*, 2013, **1**, 9973–9982.
54 B. Y. Price, G. Hardal, M. Acikgoz, S. Repp and E. Erdem, *J. Appl. Phys.*, 2015, **118**, 175705.
55 S. Gil Girol, T. Strunskus, M. Muhler and C. Woll, *J. Phys. Chem. B*, 2004, **108**, 13736–13745.
56 G. R. Li, T. Hu, G. L. Pan, T. Y. Yan, X. P. Gao and H. Y. Zhu, *J. Phys. Chem. C*, 2008, **112**, 11859–11864.
57 T. Ruf, S. Repp, J. Urban, R. Thomann and E. Erdem, *J. Nanopart. Res.*, 2016, **18**, 109.